Electron temperature critical gradient and transport stiffness in DIII-D

S.P. Smith[1], **C.C. Petty**[1], **A.E. White**[2], **C. Holland**[3]
R. Bravenec[4], **M.E. Austin**[5], **L. Zeng**[6] **and O. Meneghini**[1]

[1]General Atomics, PO Box 85608, San Diego, CA 92186-5608, USA
[2]Massachussets Institute of Technology, 77 Massachusetts Ave, Cambridge, MA 02139, USA
[3]University of California San Diego, 9500 Gilman Dr., La Jolla, CA 92093-0417, USA
[4]Fourth State Research, 503 Lockhart Dr., Austin, TX 78704, USA
[5]University of Texas at Austin, 2100 San Jacinto Blvd, Austin, TX 78712-1047, USA
[6]University of California Los Angeles, PO Box 957099, Los Angeles, CA 90095, USA

E-mail: `smithsp@fusion.gat.com`

Abstract. In a continuing effort to validate turbulent transport models, the electron energy flux has been probed as a function of electron temperature gradient on the DIII-D tokamak. In the scan of gradient, a critical electron temperature gradient has been found in the electron heat fluxes and stiffness at various radii in L-mode plasmas. The TGLF reduced turbulent transport model [G.M. Staebler *et al*, Phys. Plasmas **14**, 055909 (2007)] and full gyrokinetic GYRO model [J. Candy and R.E. Waltz, J. Comput. Phys. **186**, 545 (2003)] recover the general trend of increasing electron energy flux with increasing electron temperature gradient scale length, but they do not predict the absolute level of transport at all radii and gradients. Comparing the experimental observations of incremental (heat pulse) diffusivity and stiffness to the models' reveals that TGLF reproduces the trends in increasing diffusivity and stiffness with increasing electron temperature gradient scale length with a critical gradient behavior. The critical gradient of TGLF is found to have a dependence on q_{95}, contrary to the independence of the experimental critical gradient from q_{95}.

1. Introduction

The validation of physics models, whether analytic or numerical, against current experiments increases confidence in the predictions from those models beyond the range of current experiments (such as for predicting the performance of future fusion devices). One method of validating the models is to perform a systematic parametric scan in an experiment, to be able to compare cleanly to predictions. Using localized electron cyclotron heating (ECH) or minority ion cyclotron heating, the local electron or ion temperature gradient had previously been varied under a variety of conditions to probe the underlying physics, and provide comparisons against simulations [1, 2, 3, 4, 5, 6, 7, 8, 9]. In addition to probing the steady state energy flow, the heating systems have been pulsed in such a way as to allow for the probing of the heat pulse diffusivity and therefore stiffness of the plasma profiles [3, 4, 5, 6, 9, 10]. A previously identified regime where the prediction of plasma transport by some gyrokinetic codes is incorrect is the low-confinement regime (L-mode) edge region [11, 12, 13, 14], dubbed the "L-mode edge shortfall". Part of the inspiration for the experiments reported in the present work at the outer radii was to try to understand if the shortfall at outer radii is due to a failure of the gyrokinetic codes to predict the critical gradients and stiffness that the plasma exhibits in this region.

In this paper, we report on electron temperature gradient scale length scans in the DIII-D tokamak [15] at $\rho = 0.4$ and 0.7 with similar values of q_{95} and one scan at $\rho = 0.7$ for a lower value of q_{95}. We also report on the corresponding modeled fluxes and stiffness from the TGLF code [16] and some modeled linear growth rates and fluxes from the GYRO code [17]. For all cases we observe a critical electron temperature gradient above which electron heat transport increases more quickly with increasing gradient, and the stiffness has a clear jump from 1 to $\gtrsim$2 at the critical gradient. The scan in q_{95} reveals that TGLF energy fluxes compare better to experiment for the lower q_{95} case.

Background on the transport equations, and the meaning of fluxes, diffusivities, and stiffness are given in section 2. The experimental and modeling methods are laid out in section 3. The experimental inferences and gyrokinetic predictions of energy flux, heat pulse diffusivity, and stiffness are compared in section 4. Finally, the summary is presented in section 5.

2. Energy transport equation, flux, diffusivity, and stiffness

The heating of a toroidally axisymmetric plasma such as produced by DIII-D is governed by the energy transport equation

$$\frac{3}{2}\frac{\mathrm{d}}{\mathrm{d}t}\left(n_{\mathrm{e}}T_{\mathrm{e}}\right) + \frac{1}{V'}\frac{\mathrm{d}}{\mathrm{d}r}\left(V'Q_{\mathrm{e}}\right) = s_e. \tag{1}$$

Here n_e is the electron density, T_{e} is the electron temperature, V is the volume enclosed by the given flux surface, r is the flux surface label, Q_e is the energy flux, and s_e represents the combined energy sources (including collisional exchange from the ions and external heating). In the results presented here, the sources are assumed to be known (as calculated by various codes), and the plasma is in steady state, so the experimental power balance energy fluxes are calculated as

$$Q_{\mathrm{e}}^{\mathrm{exp}} = \frac{1}{V'} \int_0^r V' s_e \mathrm{d}r. \tag{2}$$

The energy flux can also be calculated based on models of the neoclassical and turbulent transport $Q_{\mathrm{e}}^{\mathrm{sim}} = Q_{\mathrm{e}}^{\mathrm{neo}} + Q_{\mathrm{e}}^{\mathrm{turb}}$. In this work, the model neoclassical fluxes are calculated with the NEO code [18], and the model turbulent fluxes with the TGLF [16] or GYRO [17] codes.

Let us decompose the power balance (PB) energy flux (whether model or experimental) into two parts

$$Q_e^{\mathrm{PB}} = -n_e D_e^{\mathrm{PB}} \nabla T_e + F, \tag{3}$$

where $\partial F / \partial \nabla T_e = 0$. Let us define the heat pulse diffusivity as [6]

$$D_e^{\mathrm{HP}} = -\frac{1}{n_e} \frac{\partial Q_e^{\mathrm{PB}}}{\partial \nabla T_e} = \frac{\partial}{\partial \nabla T_e} (D_e^{\mathrm{PB}} \nabla T_e). \tag{4}$$

From the final form of (4), the power balance diffusivity D_e^{PB} can be solved as

$$D_e^{\mathrm{PB}} = \frac{1}{\nabla T_e} \int_0^{\nabla T_e} D_e^{\mathrm{HP}} \mathrm{d}(\nabla T_e). \tag{5}$$

The stiffness is then defined as

$$S = D_e^{\mathrm{HP}} / D_e^{\mathrm{PB}}. \tag{6}$$

3. Methods

3.1. Experimental

In the DIII-D tokamak, we have employed the electron cyclotron heating systems (gyrotrons) to locally heat the electrons. By aiming all six of the gyrotrons at the same initial location, then moving the gyrotrons one by one to a second location in subsequent discharges, a scan in electron temperature gradient ∇T_e can be realized midway between the two aiming locations. Using this method, we have scanned ∇T_e at relatively constant T_e by depositing ECH power on either side of $\rho = 0.4$ [figure 1(a)], $\rho = 0.6$ [6, 8, 9], and $\rho = 0.7$ [figure 1(b,c)], where ρ is the normalized toroidal flux coordinate. The toroidal field across these scans is 1.98–2.02 T, with an aspect ratio of $R/a = 2.14$. The scans at $\rho = 0.4, 0.6$ had 0.8 MA plasma current; the scans at $\rho = 0.7$ had currents of 0.6 and 1.2 MA for q_{95} values of 8.6 and 4.3, respectively.

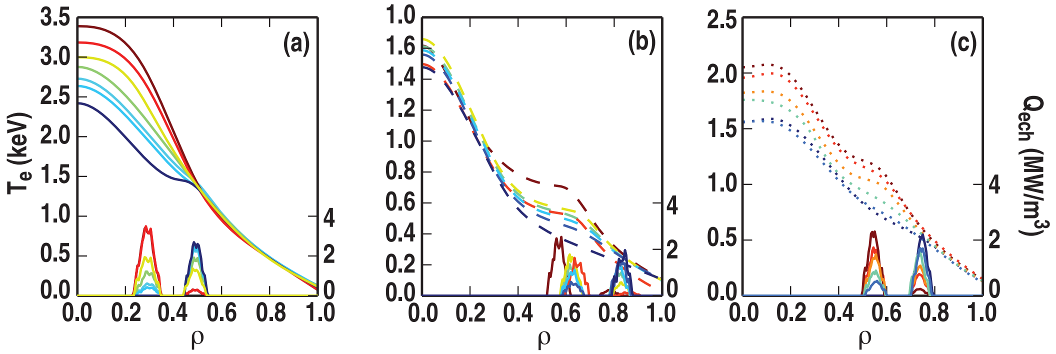

Figure 1. Spline fits to electron temperature T_e measured by the electron cyclotron emission diagnostic (left scales) and calculated volumetric electron cyclotron heating (right scales) vs normalized toroidal flux ρ for a) the $\rho = 0.4$ case, b) the $\rho = 0.7$, $q_{95} = 8.6$ case, and c) the $\rho = 0.7$, $q_{95} = 4.3$ case.

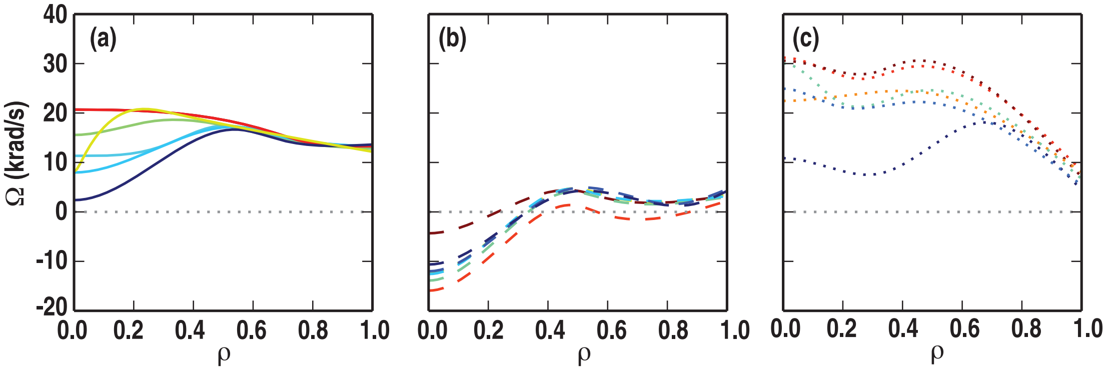

Figure 2. Spline fits to Carbon VI toroidal rotation measurements Ω vs ρ for the a) $\rho = 0.4$ case b) $\rho = 0.7$ $q_{95} = 8.6$ case and c) $\rho = 0.7$ $q_{95} = 4.3$ case. Line coloring is the same as that for the T_e profiles of figure 1.

In these discharges, there is no beam heating, such that there is no external beam torque on the plasma, nor any central particle fueling. It is interesting to observe that the plasma rotation can depend on q_{95} or even just the ECH deposition location. In figure 2 the toroidal rotation profile fits are shown for the $\rho = 0.4$ case (a), the $\rho = 0.7$ $q_{95} = 8.6$ case (b), and the $\rho = 0.7$ $q_{95} = 4.3$ case (c). The color coding for the lines is the same as the corresponding temperature profiles in figure 1. In figure 2(a,c), there is a clear trend of decreasing inner rotation with decreasing inner ECH deposition (red to blue). Comparing the cases in figure 2(b,c), there is a rotation reversal for the change in plasma current from 1.2 MA in (b) to 0.6 MA in (c). However, this is not the only parameter that is changing. The profiles of the electron density n_e and ion temperature T_i are shown in figure 3, where it is seen that the $q_{95} = 8.6$ (dashed) and $q_{95} = 4.3$ (dotted) n_e and T_i are different and could also contribute to the rotation reversal. To

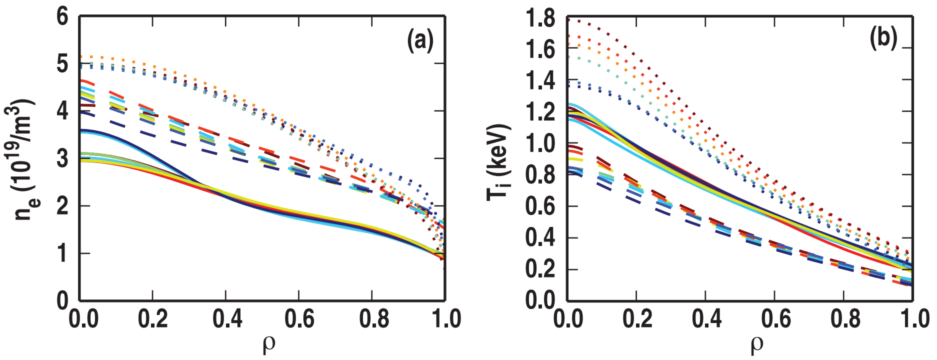

Figure 3. Electron density n_e (a) and ion temperature T_i (b) vs ρ for the (solid) $\rho = 0.4$ case; (dashed) $\rho = 0.7$, $q_{95} = 8.6$ case; and (dotted) $\rho = 0.7$, $q_{95} = 4.3$ case.

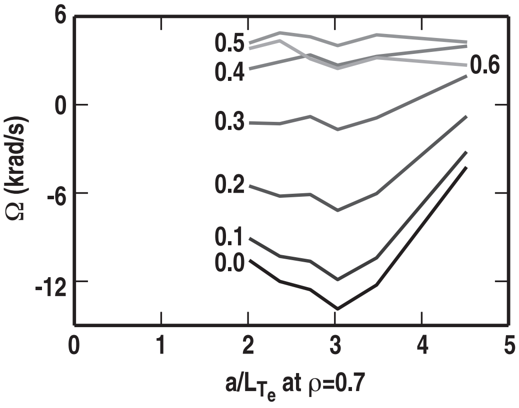

Figure 4. The angular rotation of figure figure 2(b) at the labeled radii ($\rho = 0 \ldots 0.6$) vs a/L_{T_e} evaluated at $\rho = 0.7$.

better understand the dependence on the ECH deposition of the rotation in case b, the angular rotation at discrete radial points $\rho = 0, 0.1, 0.2 \ldots 0.6$ is shown versus the temperature gradient scale length at $\rho = 0.7$ in figure 4 as the power deposited inside $\rho = 0.7$ is increased. For the inner radii, there is a clear change in dependence on a/L_{T_e} at around $a/L_{T_e} = 3$.

One of the gyrotrons was always left in the outer location and modulated at 28 Hz for all cases. This modulation allows the experimental heat pulse diffusivity to be determined [6].

3.2. Simulation

The experimental profiles were used as inputs to the gyrofluid code TGLF [16] and to the gyrokinetic code GYRO [17] to obtain predictions of the microstability linear growth rates or turbulence driven plasma transport fluxes. The TGLF results presented here

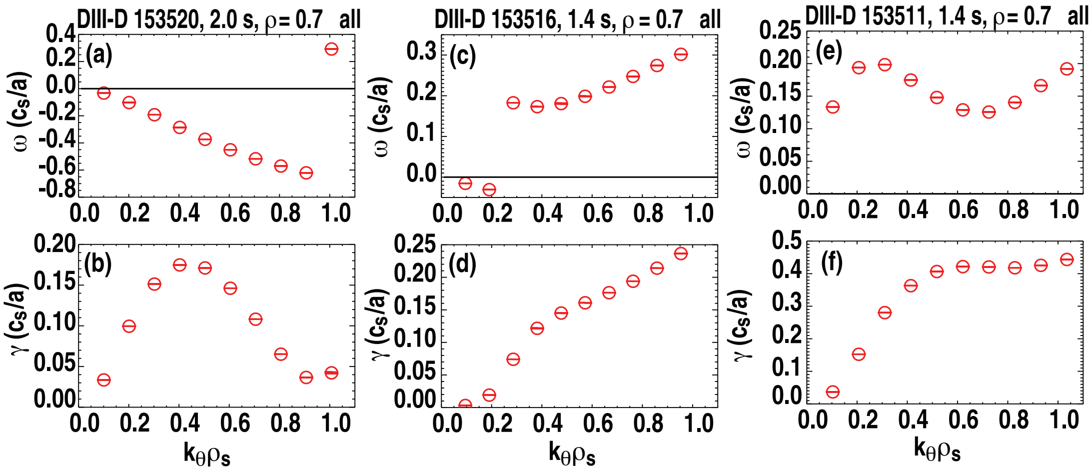

Figure 5. GYRO predicted linear frequencies (top) and growth rates (bottom) for the smallest (left), moderate (middle) and highest (right) T_e gradients for the $\rho = 0.7$ $q_{95} = 8.6$ case. Positive frequency indicates a mode in the electron diamagnetic direction.

include the recent recalibration of the model [19].

The linear growth rates and frequencies for the lowest and highest gradients (left and right panels) and a moderate gradient (middle panel) for the $\rho = 0.7$ $q_{95} = 8.6$ cases are in figure 5. Note the change in frequency of the dominant mode as the gradient is increased from the lowest gradient; this would indicate a change from an ITG type mode to a more TEM type mode. The change in mode behavior is supported by the rotation profiles of figure 4, where the intrinsic torque driven rotation has a different behavior at lower a/L_{T_e} than at higher a/L_{T_e}. That the growth rate continues to increase with increasing ∇T_e indicates that the mode is a ∇T_e driven TEM. Also, the growth rate is peaked at low $k_\theta \rho_s$ (ion turbulence scales) for the lowest gradient, whereas for the higher gradients, there is not a peak in growth rates, within the range of $k_\theta \rho_s$ calculated. Even without a well-defined peak, the nonlinear simulations can be well resolved in $k_\theta \rho_s$ space because the fluxes tend to decrease as γ/k_θ^2.

Nonlinear electrostatic collisional GYRO simulations without flow were performed to obtain the fluxes for the same cases as given in figure 4. The smallest and largest gradient case simulations used 16 modes in the binormal direction k_θ, with $0 < k_\theta \rho_* < 1$. The middle gradient case used 24 modes with $0 < k_\theta \rho_* < 1.5$. All simulations had 240 points for velocity space resolution (2 signs×10 pitch angles× 12 energies), with box size $\sim 100\rho_*$ and 192 points in the radial discretization.

4. Comparisons

Part of the motivation for performing these experiments was to be able to compare the experimental results with simulations to validate the models in the simulations. Here we provide comparisons of the fluxes, heat pulse diffusivities, and stiffnesses.

4.1. Power balance fluxes

The experimental power balance fluxes are calculated with the ONETWO code [20, 21], which accesses the ray tracing code TORAY-GA [22] to calculate the ECH power deposition. In figure 6, the electron Q_e (a,d,g), ion Q_i (b,e,h), and summed $Q_e + Q_i$ (c,f,i) energy fluxes at the appropriate radii are shown versus the normalized ∇T_e scale length a/L_{T_e} for the $\rho = 0.4$ case (a,b,c), the $\rho = 0.7$ $q_{95} = 8.6$ case (d,e,f), and the $\rho = 0.7$ $q_{95} = 4.3$ case (g,h,i). The experimentally calculated fluxes are shown as $\circ$. The sum of the TGLF fluxes (for turbulence) and NEO fluxes (for neoclassical, but usually negligible for electrons) are given as $\square$. The sum of the GYRO fluxes (for turbulence) and NEO fluxes are given as $\diamond$, for the smallest, medium, and largest gradients of the $\rho = 0.7$ $q_{95} = 8.6$ case. It is reassuring that the GYRO and TGLF predicted fluxes are very close to each other in these conditions, as the TGLF model has been tuned in its saturation rule to obtain results similar to GYRO for a separate standard case. Finally, there is a numerical scan of a/L_{T_e} for TGLF shown as the dashed curve, whose other parameters come from the experimental parameters of the point with the second highest gradient.

As expected, the experimental Q_e depend strongly on a/L_{T_e} for all of the cases considered here. The TGLF Q_e are similar in magnitude to the experimental Q_e at the lower a/L_{T_e}, and the TGLF Q_e also depend strongly on a/L_{T_e}. However, for the $\rho = 0.4$ case the TGLF dependence is stronger than experiment; for the $\rho = 0.7$ case at higher q_{95} the TGLF dependence is weaker than experiment; and for the $\rho = 0.7$ case at lower q_{95}, the TGLF dependence is very similar to experiment. There is a lack of TGLF "heat pinch" at the lowest a/L_{T_e} for the $\rho = 0.7$ higher q_{95} case.

The experimental Q_i depend slightly on a/L_{T_e} for the higher q_{95} $\rho = 0.7$ case, but is fairly independent for the other two cases. For the $\rho = 0.7$ cases, the TGLF Q_i are independent of a/L_{T_e}, with the lower q_{95} fluxes of similar magnitude to experiment (like

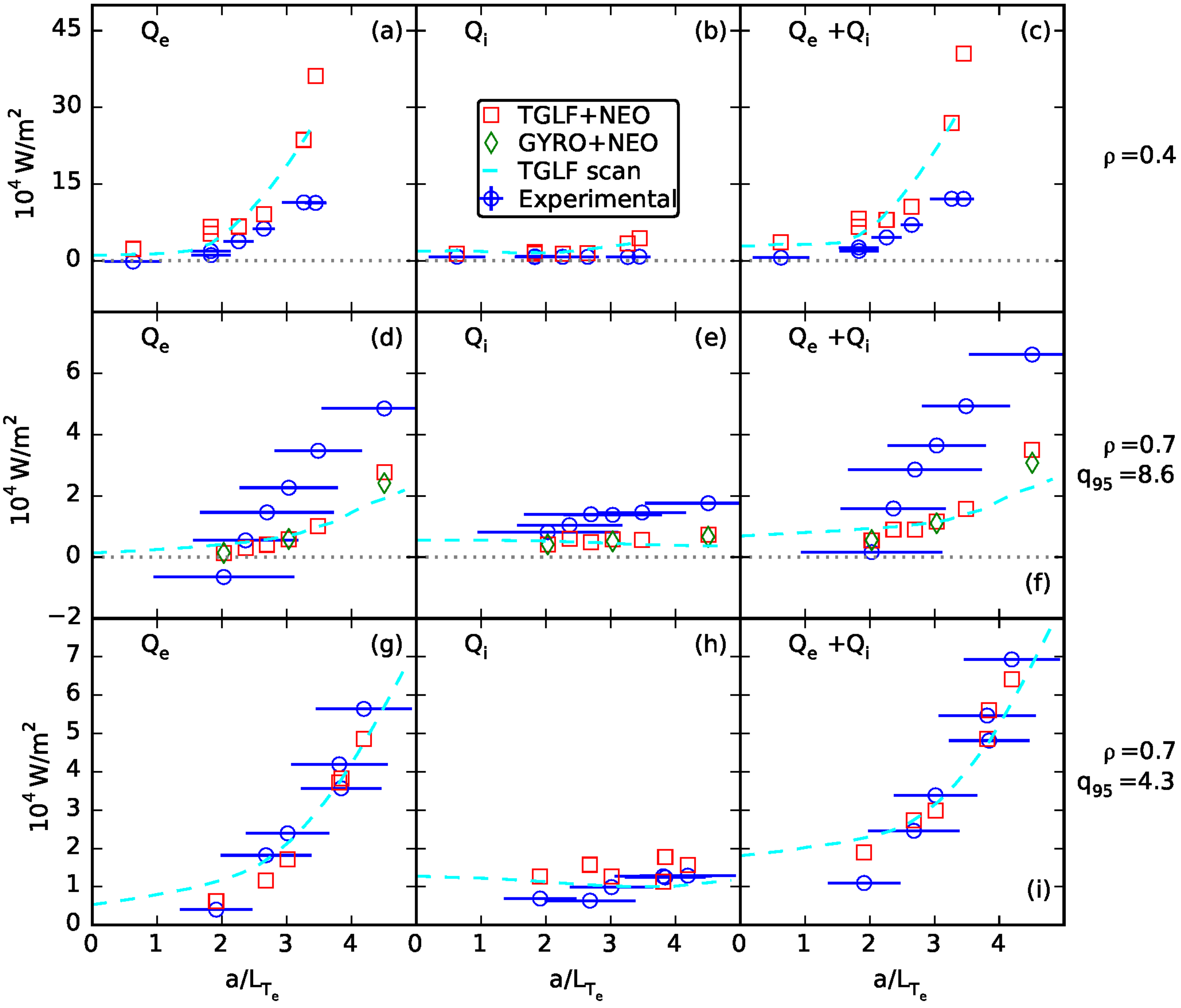

Figure 6. The electron (a,d,g), ion (b,e,h) and total (c,f,i) energy fluxes vs the electron temperature gradient scale length for the $\rho = 0.4$ case (a,b,c), the $\rho = 0.7$ $q_{95} = 8.6$ case (d,e,f), and the $\rho = 0.7$ $q_{95} = 4.3$ case (g,h,i). The ○ are experimental points; the □ are predictions from TGLF; the ◊ are predictions from GYRO; the dashed curves are TGLF predictions from a scan in a/L_{T_e} based on the experimental conditions corresponding to the second largest value of a/L_{T_e} for each case.

the electron fluxes), but the higher q_{95} case TGLF fluxes are smaller than experiment.

Summing the ion and electron fluxes eliminates the fluxes due to collisional exchange and reveals that TGLF predicts the summed energy flux fairly well for the lower q_{95} case at $\rho = 0.7$, but underpredicts the flux for the higher q_{95} case, consistent with the motivation to further investigate the "L-mode edge shortfall", where we see here that the shortfall is stronger at larger a/L_{T_e}. For the $\rho = 0.4$ case, there is also a trend with

a/L_{T_e} for summed flux, and TGLF tends to overpredict this flux by as much as 4× at the highest gradient.

4.2. Diffusivities and Stiffness

In the experiment, the heat pulse diffusivity D_e^{HP} can be extracted from Fourier analysis of the ECE T_e measurements, which are modulated by the single modulated gyrotron [6]. For the TGLF code, D_e^{HP} is obtained by modifying the ∇T_e input to the code by 10% to obtain an incremental $Q_e^{\mathrm{PB,inc}}$, then taking the ratio $(Q_e^{\mathrm{PB,inc}} - Q_e^{\mathrm{PB}})/(1.1\nabla T_e - \nabla T_e)/n_e$. In both the experimental and TGLF cases D_e^{PB} is calculated from D_e^{HP} according to (5), where the value of $D_e^{\mathrm{HP}}\big|_{\nabla T_e=0}$ is defined as $D_e^{\mathrm{HP}}\big|_{\nabla T_e=\min(\nabla T_e)}$.

In figure 7 are shown the experimental ○ + and TGLF □ D_e^{HP} (panels a and d), D_e^{PB} (panels b and e), and stiffness (panels c and f) for the $\rho = 0.7$ $q_{95} = 8.6$ case (panels a, b, and c) and $\rho = 0.7$ $q_{95} = 4.3$ case (panels d, e, and f). The dashed curve is obtained from the strict ∇T_e scan of TGLF, shown as the dashed curve in figure 6. The TGLF results agree with the broad experimental trends of increasing D_e^{HP} and D_e^{PB} with increasing a/L_{T_e}. Both experiment and TGLF exhibit a critical gradient behavior above which the stiffness increases rapidly. Also shown as solid curves are a fit to D_e^{PB} and resulting D_e^{HP} and stiffness for each case for a model having two linear segments joined at $a/L_{T_e}^{crit}$. To wit,

$$D_e^{\mathrm{PB,fit}} = C_1(a/L_{T_e} - a/L_{T_e}^{crit})H(a/L_{T_e} - a/L_{T_e}^{crit}) + C_2. \tag{7}$$

There is a corresponding $D_e^{\mathrm{HP,fit}}$ consistent with (4), and a fit stiffness $D_e^{\mathrm{HP,fit}}/D_e^{\mathrm{PB,fit}}$, such that the fit is simultaneously to the experimental D_e^{PB}, D_e^{HP}, and stiffness (likewise for the TGLF quantities). The parameters from the best fits are given in Table 1. From these parameters, the TGLF model has a smaller critical gradient than experiment, and in the case of the $q_{95} = 8.6$ it also has much lower baseline transport (characterized by the C_2 parameter). The values of $a/L_{T_e}^{crit}$ from the fits are consistent with the stiffness transitioning from below 2 to above 2 at these values of a/L_{T_e}. The increase in stiffness at the critical gradient is also consistent with the change in character of the linear growth rates from an ion mode to an electron mode.

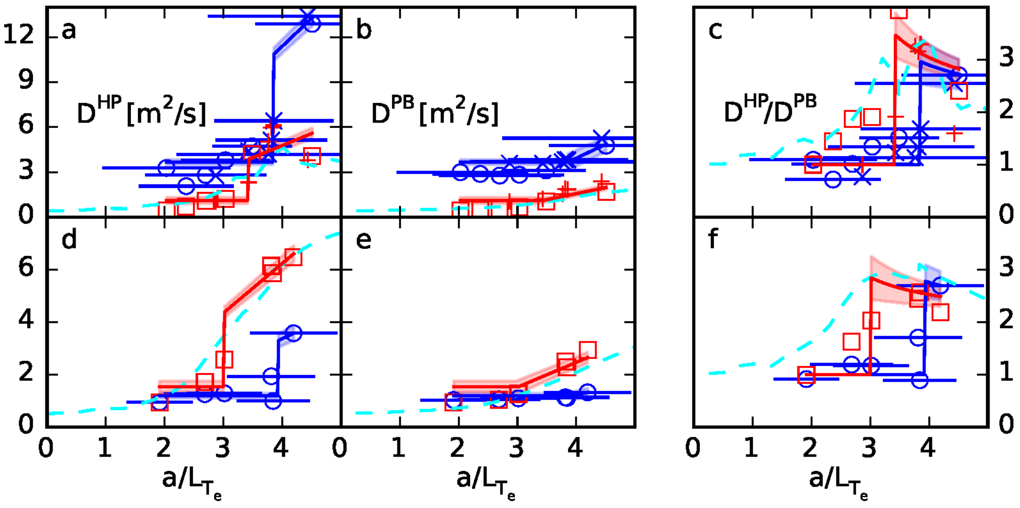

Figure 7. Experimental ○ ×and TGLF □ heat pulse diffusivity [panels (a) and (d)], power balance diffusivity [panels (b) and (e)], and stiffness [panels (c) and (f)] vs a/L_{T_e} for the $\rho = 0.7$ $q_{95} = 8.6$ case [panels (a-c)] and $\rho = 0.7$ $q_{95} = 4.3$ case [panels (d-f)].

Table 1. Value and uncertainty of the parameters of the best fit [see equation (7)] for experiment or TGLF for the two different cases of q_{95} at $\rho = 0.7$.

	Experiment			TGLF		
q_{95}	C_1	C_2	$a/L_{T_e}^{\mathrm{crit}}$	C_1	C_2	$a/L_{T_e}^{\mathrm{crit}}$
8.6	1.9± 0.2	3.7± 0.2	3.9± 0.3	0.80± 0.06	1.1± 0.2	3.4± 0.3
4.3	0.54± 0.08	1.2± 0.1	3.9± 0.3	0.94± 0.08	1.5± 0.2	3.0± 0.3

5. Conclusion

In the DIII-D tokamak, we have performed scans in a/L_{T_e} at various radii, with a sufficient range to see that a critical gradient has been exceeded to dominantly excite TEM more than ITG type turbulence based on the gyrokinetic linear growth rates. The change in nature of the dominant instability can be seen by its effect on the rotation profile and by the increased dependence of the energy fluxes on a/L_{T_e} leading to an increase in stiffness of the electron heat flux with regard to a/L_{T_e}. The TGLF and GYRO models predict trends in electron energy fluxes similar to that inferred from experiment, but the ion energy fluxes are underpredicted for the higher q_{95} $\rho = 0.7$ case. Focussing on the electron transport, the trends of increasing heat pulse diffusivity and stiffness from TGLF compares well to the experimental observations. A critical gradient is seen in experiment that is independent of the q_{95} condition; this independence is not seen in TGLF. For the $q_{95} = 4.3$ case, TGLF matches the experimental baseline transport fairly well, but in the experiment the baseline transport increases at $q_{95} = 8.6$ and this trend is not reproduced by TGLF, where actually the baseline transport is lower at the higher q_{95}. A shortfall in the prediction of electron and ion energy fluxes exists in the higher q_{95} $\rho = 0.7$ case at the higher a/L_{T_e} achieved.

The results here reported bring into question the absolute validity of TGLF for the plasmas here studied with $T_e \gtrsim T_i$. The TGLF critical gradients depend on q_{95}, which is not seen in experiment. Future experiments are expected to operate near the critical gradient across the plasma, such that a more precise and accurate determination of the critical gradients will be vital for determining the predictions of profiles in those devices. While the linear equations that TGLF solves are well defined, the saturation rule used to combine the growth rates into a flux should be adjusted to better represent the influence of high-k turbulence on total flux, where recent work [13] has shown that including both ion scales and electron scales in a given GYRO simulation can produce drastic increases in both electron and ion energy fluxes.

Acknowledgments

This work was facilitated by the OMFIT framework. This material is based upon work supported in part by the U.S. Department of Energy, Office of Science, Office of Fusion Energy Sciences, using the DIII-D National Fusion Facility, a DOE Office of Science user facility, under Awards DE-FC02-04ER54698, DE-FC02-99ER54512, DE-FG02-08ER54871, DE-FG03-97ER54415, and DE-FG02-08ER54984. DIII-D data shown in this paper can be obtained in digital format by following the links at https://fusion.gat.com/global/D3D_DMP.

References

[1] DeBoo J.C. et al 2005 *Nucl. Fusion*, **45** 494

[2] Peeters A.G., Angioni C., Apostoliceanu M., Jenko F., Ryter F. and the ASDEX Upgrade Team 2005 *Phys. Plasmas* **12** 022505

[3] Ryter F., Angioni C., Peeters A.G., Leuterer F., Fahrbach H.-U. and Suttrop W. 2005 *Phys. Rev. Lett.* **95** 085001

[4] Mantica P. et al 2009 *Phys. Rev. Lett.* **102** 175002

[5] P. Mantica, et al. *Phys. Rev. Lett.* **107** 135004

[6] DeBoo J.C. et al 2012 *Phys. Plasmas* **19** 082518

[7] Baiocchi B., Mantica P., Giroud C., Johnson T., Naulin V., Salmi A., Tala T., Talas M. and Contributors JET-EFDA 2013 *Plasma Phys. Controlled Fusion* **55** 025010

[8] Hillesheim J.C. et al 2013 *Phys. Rev. Lett.* **110** 045003

[9] Holland C. et al 2013 *Nucl. Fusion* **53** 083027

[10] Ryter F. et al 2011 *Nucl. Fusion* **51** 113016

[11] Holland C., White A.E., McKee G.R., Shafer M.W., Candy J., Waltz R.E., Schmitz L. and Tynan G.R. 2009 *Phys. Plasmas* **16** 052301

[12] Rhodes T.L. et al 2011 *Nucl. Fusion* **51** 063022

[13] Howard N.T., White A.E., Greenwald M., Holland C. and Candy J. 2014 *Phys. Plasmas* **21** 032308

[14] Told D., Jenko F., Görler T., Casson F.J., Fable E. and ASDEX Upgrade Team 2013 *Phys. Plasmas* **20** 122312

[15] Luxon J.L. 2002 *Nucl. Fusion* **42** 614

[16] Staebler G.M., Kinsey J.E. and Waltz R.E. 2007 *Phys. Plasmas* **14** 055909

[17] Candy J. and Waltz R.E. 2003 *J. Comput. Phys.* **186** 545

[18] Belli E.A. and Candy J. 2008 *Plasma Phys. Controlled Fusion* **50** 095010

[19] Staebler G.M. 2014 *Private Communication*

[20] Pfeiffer W.W., Davidson R.H., Miller R.L. and Waltz R.E. 1980 ONETWO: A computer code for modeling plasma transport in tokamaks. General Atomics Report GA-A16178

[21] St. John H., Taylor T.S., Lin-Liu Y.R. and Turnbull A.D. 1994 *Plasma Physics and Controlled Nuclear Fusion Research 1994*, vol 3 (International Atomic Energy Agency, 1994) p 603

[22] Matsuda K. 1989 *IEEE Trans. on Plasma Science* **17** 6

[23] Meneghini O. et al 2015 (submitted to Nucl. Fus. for inclusion in the IAEA2014 issue)